# Final Report Fermilab Italian Student Program

Michele Mormile

# Contents

# Introduction

I participated to the 2019 Fermilab Italian Student Program under the supervision of Anadi Canepa and Lorenzo Uplegger.

I worked with the Fermilab research group that is involved with the R&D of the CMS Outer Tracker. The Compact Muon Solenoid (CMS) is a a general-purpose detector located at the Large Hadron Collider (LHC), the world's most powerful particle accelerator. In the next years LHC will undergo the High-Luminosity LHC upgrade, which will bring its luminosity from $1 \times 10^{34}$ cm$^{-2}$ s$^{-1}$ to $1.5 \times 10^{34}$ cm$^{-2}$ s$^{-1}$. This increase in luminosity will require an upgrade of CMS as well, in order to comply with the augmented rate of particles which will cross the detector.

The CMS tracker is a detector, composed of various modules made of silicon pixel trackers and silicon strip trackers, whose aim is to reconstruct the trajectories of the particles produced by the collisions in LHC.

The tracker is ideally divided in Inner Tracker and Outer Tracker. The HL-LHC upgrade put important challenges in the designing of the tracker. It will have to withstand the irradiation of a large fluence of particles, without suffering a too severe deterioration of its performance.

In addition to this, in order to comply with the increased rate of events that CMS will need to detect, the tracker will be exploited for triggering at the fully hardware Level 1 Trigger, in contrast to the current tracker, whose data are only used for the software High-Level Trigger. This feature is managed by the "stub logic", which will be explained in chapter 2.

During the months of August and September at Fermilab I carried out the data analysis of three test beam runs performed in the last two years on the 2S Outer Tracker Minimodules. The 2S Minimodule consists of two silicon strip trackers placed one upon the other with the strips kept parallel.

The three test beam runs differ with regard to the fluence that the minimodule undertook:

- Unirradiated
- $2 \times 10^{14}$ $neq/cm^2$
- $4.4 \times 10^{14}$ $neq/cm^2$

By analizing the data and comparing the results of these different data taking runs, I have been able to describe the radiation hardness of the sensor, as well as its trigger effectiveness.

# Chapter 1

# The Compact Muon Solenoid

## 1.1 The Compact Muon Solenoid

### 1.1.1 The Large Hadron Collider

The *Large Hadron Collider* (LHC) is the world's largest and most powerful particle accelerator. It consists of a 27-kilometre ring of superconducting magnets with a number of accelerating structures to boost the energy of the particles along the way.[1] It is used to accelerate and collide protons and heavy ions at four locations along the ring, where four detectors are located:

- **CMS**
- **ATLAS**
- **ALICE**
- **LHCb**

The LHC collides protons with a center-of-mass energy of 13 TeV and an instantaneous luminosity of $1.5 \times 10^{34}$ cm$^{-2}$ s$^{-1}$.[2]

In 2024 the LHC will undergo the High Luminosity-LHC upgrade which will enable instantaneous peak luminosities of $5 \times 10^{34}$ cm$^{-2}$ s$^{-1}$, or even $7.5 \times 10^{34}$ cm$^{-2}$ s$^{-1}$, in the ultimate performance scenario. [3] This will allow ATLAS and CMS to collect integrated luminosities of the order of 3000 fb$^{-1}$ during the planned lifetime of 10 years, as opposed to the 300 fb$^{-1}$ collected so far.

### 1.1.2 The Compact Muon Solenoid

The *Compact Muon Solenoid* (CMS) is a general-purpose particle detector located at the LHC. It was designed to observe the products of the collisions produced by the accelerator in order to study a broad spectrum of physics. It is able to detect Standard Model phenomena as well as events that could lead to new physics beyond standard model.[4]

It consists of multiple layers of subdetectors (fig. 1.1):

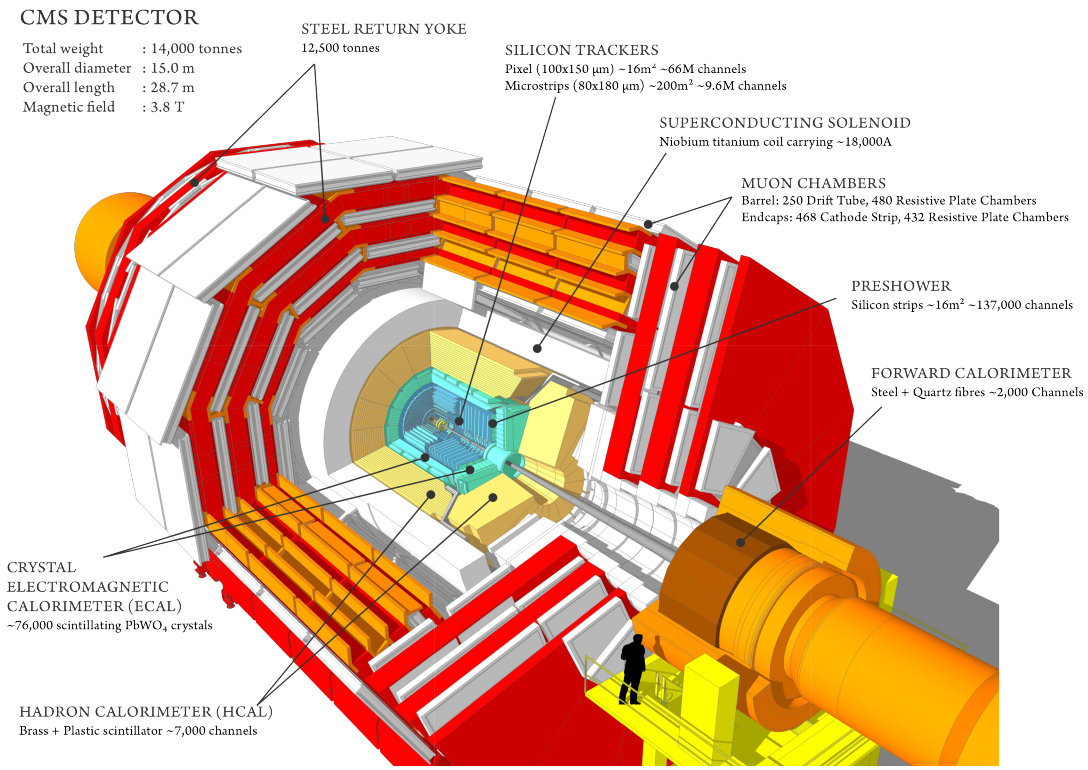


**Figure 1.1:** A schematic view of the subdetectors which compose CMS. [5]

- **Tracker**

  It is the detector most close to the collision points. It reconstructs the path of charged particles so to measure their momenta and to find the interaction vertices.

- **Calorimeters**

  They are used to measure the energy of the particles. There are two types of calorimeter: the smaller electromagnetic calorimeter detects electrons and photons and the larger hadron calorimeter detects hadronic particles, such as protons and neutrons.

- **Muon chambers**

  They are used to reconstruct the track of muons, which are the only ones penetrating enough to escape from the detector.

Between the hadron calorimeter and the muon chambers is located a large superconducting solenoid made of niobium titanium which provides the inner part of the detector with a 3.8 T magnetic field. This magnetic field bends the paths of charged particle according to their momenta, allowing this latter to be indirectly measured from the reconstruction of the trajectory of the particles.

# Chapter 2

# The Outer Tracker

During the Italian Student Program I worked with the Fermilab research group that is involved with the R&D of the CMS Outer Tracker. In this chapter, after talking about silicon detectors, I will give a short summary of the reasons that make necessary an upgrade of the detector for the HL-LHC.

## 2.1 Silicon Trackers

The present tracker used in CMS is composed of silicon strip detectors and silicon pixel detectors. The working principle of a strip sensor is displayed in figure 2.1. A silicon detector consists of a p-n junction to which a reverse bias voltage is applied. The latter creates an electric field in the detector which causes it to be fully depleted of charge carriers, so that no current flows in the junction. When a charged particle passes through the sensor, it undergoes multiple Coulomb scattering with the electrons of the bulk, kicking them off their atoms and effectively creating couples of free electrons and electronic holes along its path. These charge carriers are then collected at the electrodes of the detectors, thanks to the electric field present in the bulk. According to the positions of the electrodes which collect the charge, it is possible to reconstruct the position of the particle which crossed the detector.

## 2.2 Radiation Damage

The increased luminosity of the LHC will result in an increase of the number of particles passing through the detectors. In the case of silicon detectors, this causes radiation damage, which degrades the performances of the sensor, by decreasing the amount of charge collected. This is due to the fact that particles crossing the bulk of the sensor can release enough energy to displace atoms from their positions in the crystal lattice. These defects in the structure correspond to energy levels present in the gap between the valence and conduction bands. These levels act as electron traps,in which electrons and holes fall before they can be collected at the electrodes, lowering the strength of the signal, as it will be shown in chapter 3.

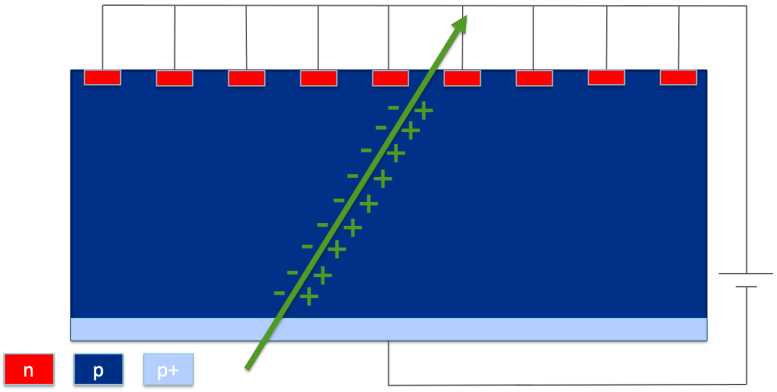


**Figure 2.1:** When a charged particle passes through a silicon strip tracker, it sets free charge carriers which are then collected by the strips.

This radiation damage can be mitigated by heat annealing. When silicon is kept at high temperature, some of the displaced atoms tend to migrate back to their positions in the crystal lattice, thus diminishing the number of energy gap levels.

The new tracker modules will thus need to have reliable performances even after being crossed by high fluences of particles.

## 2.3 The Outer Tracker

After the upgrade, the CMS Tracker will be divided in Inner Tracker (composed of pixel detectors) and Outer Tracker. The Outer Tracker will be composed of two modules (fig. 2.2):

- **PS module:**

  It will be arranged in the inner part of the Outer Tracker and is composed of two layers of silicon tracker: a strip detector and a pixel detector.

- **2S module:**

  It will compose the outer layer of the CMS Tracker and it consists of two silicon strip detector placed one upon the other, with parallel strips.

Another requirement dictated by the increase in luminosity is an increased trigger capability, in order to keep the trigger rate at an acceptable level while not compromising physics potential.

The CMS trigger consists of a Level 1 (L1) hardware trigger, and a High-Level Trigger (HLT). Currently, the information from the tracker are used only for HLT. After the upgrade, the tracker will also be exploited at L1 trigger to put a threshold on the transverse momentum $p_T$ of the particle, thanks to the "stub" logic.

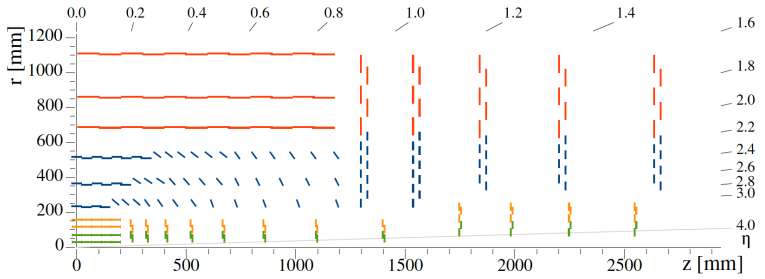


**Figure 2.2:** Sketch of one quarter of the tracker layout in r-z view. In the Inner Tracker the green lines correspond to pixel modules made of two readout chips and the yellow lines to pixel modules with four readout chips. In the Outer Tracker the blue lines represent the PS modules and the red lines represent the 2S modules. [2]

## 2.4 The Stub Logic

According to electromagnetism, a charged particle in a uniform magnetic field sees its trajectory bent with a radius of curvature:

$$r = \frac{p_T}{qB} \tag{2.1}$$

where $q$ is the charge of the particle and $B$ is the magnetic field.

Therefore, each charged particle that passes through the CMS detector has its path bent by the 3.8 T magnetic field created by the solenoid. Nevertheless, particles with high $p_T$ will follow an almost undisturbed trajectory and do not deviate appreciably from the radial direction, while the ones with low $p_T$ undergo a more evident bending and their trajectories acquire a considerable azimuthal component.

Hence, as shown in figure 2.3, a particle with high $p_T$ passing through the 2S module creates clusters of fired strips that are close on the $\Phi$ axis. On the other hand, if the $p_T$ is low, the azimuthal component of the trajectory that the particle acquires on its way to the Outer Tracker causes it to fire clusters that are far apart on the two detectors of the module. In the first case, we say that we have a "stub" and a trigger output is sent out. We can set the threshold in $p_T$ for the stub by adjusting the acceptable distance in strips between the clusters fired in the two detectors, according to the formula:

$$p_T = \frac{2qB}{R} \frac{\frac{d}{h}}{\sqrt{\left(\frac{d}{h}\right)^2 + 1}} \tag{2.2}$$

where $R$ is the distance of the module from the beampipe, $h = 1800\ \mu m$ is the distance between the strips in the two detectors and $d$ is the distance between the clusters in the two detectors along the $\phi$ axis, and is measured in units of strip pitch (90 $\mu$m).

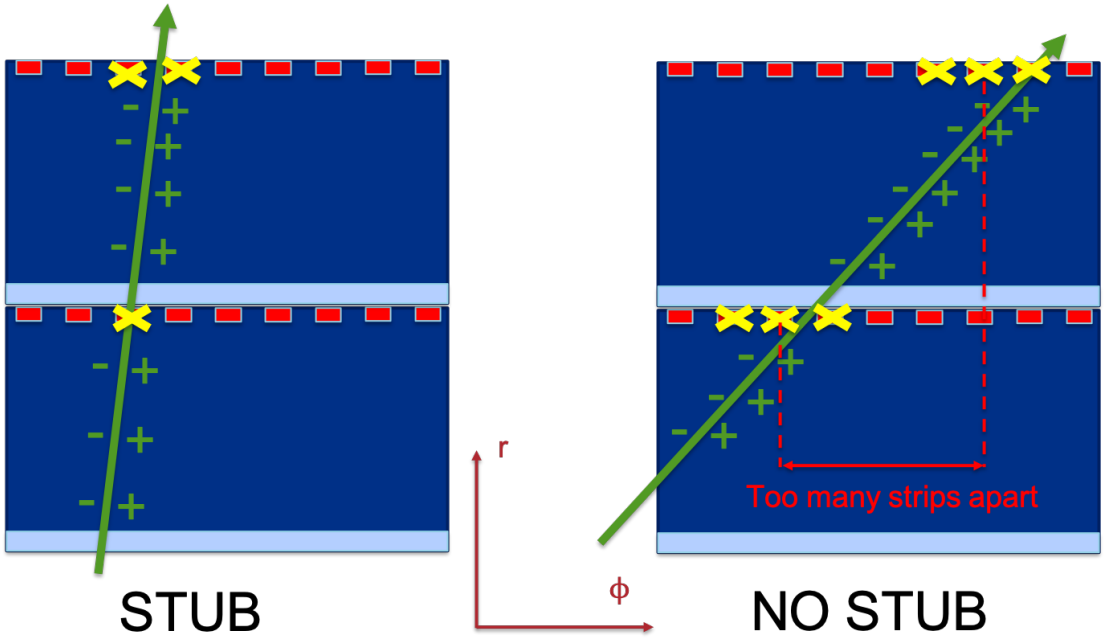


**Figure 2.3:** When a particle is emitted with high $p_T$ it doesn't deviate much from the radial direction and generates a stub in the 2S module. A particle with low $p_T$ acquires a consistent azimuthal component and its passage through the detector does not result in a stub.

# Chapter 3

# Test Beam Analysis

During my time at Fermilab I carried out the data analysis of the test beams performed on a 2S Outer Tracker Minimodule. The minimodule consists of two layers of strip detectors, as descripted in chapter 2. Each layer is provided with 254 strips. The minimodule is completed by a chip which reads every strip independently and is able to determine whether the charge collected by a channel is higher than a set threshold. The chip clock has a 25 ns period. The two different layers of strip detector are called "seed sensor" and "correlated sensor", according to their roles in the stub logic: after a hit is detected in the seed sensor, the chip checks for a possible stub on the correlated sensor within the set strip distance.

The 2S minimodule underwent three test beams:

- **November 2017**

  The detector was tested for the first time. In this report I will refer to this data taking period as the one with the "unirradiated sensor"

- **June 2018**

  After the first test beam, the detector was sent to the Rhode Island Nuclear Science Center to be irradiated with neutrons up to $2 \times 10^{14}$ $neq/cm^2$. In this period, which I will refer to as the one with the "half irradiated sensor", the detector was tested both before and after an annealing process, i.e., it was kept at 60 °C for two hours.

- **December 2018**

  The detector was then sent again to the Nuclear Science Center to be irradiated with a fluence of $2.4\times10^{14}$ $neq/cm^2$, for a total of $4.4\times10^{14}$ $neq/cm^2$, which is fairly higher than the $3.0\times10^{14}$ $neq/cm^2$ that the detector is foreseen to undertake. [2] I will refer to as the one with the "fully irradiated sensor".

## 3.1 The Test Beam

The test beams were carried out at the Fermilab Test Facility, using protons accelerated to an energy 120 GeV by the Main Injector accelarator. The facility

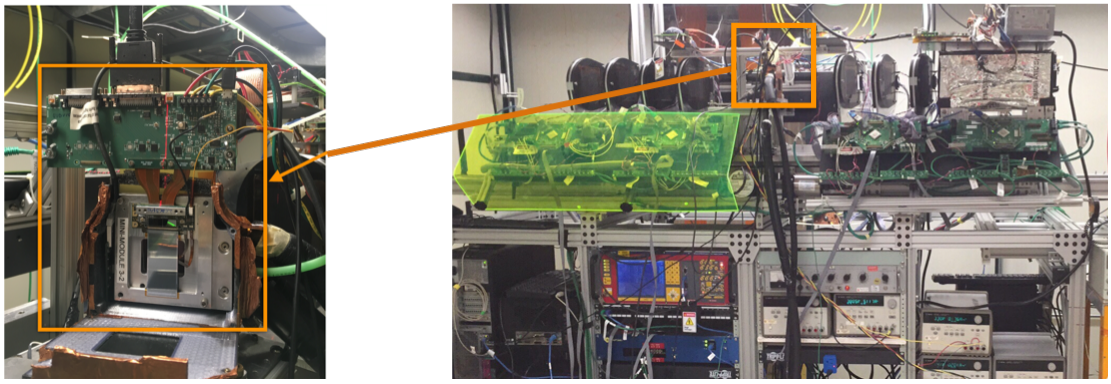

**Figure 3.1:** In the right picture, it is displayed the telescope at the Fermilab Test Beam Facility. In the left picture, it is shown the 2S module in the middle of the telescope.

is equipped with a tracking telescope and a scintillator to provide the trigger (fig. 3.1). The telescope setup was different for the different data taking runs:

- **November 2017**: the telescope was only composed of pixel detectors
- **June and December 2018:** the telescope was composed of both pixel and strip detectors.

Nonetheless, the resolution was very similar in each case ($\sim 7\ \mu m$)

We used the Monicelli software to reconstruct the tracks of the particles passing through the telescope and to evaluate the positions and orientations of the telescope detectors and the minimodule. We reconstructed only tracks which went undetected by no more than 2 telescope planes and with no more than 2 clusters on each plane. In addition, we only accepted events when the cluster location on the minimodule was within 135 $\mu$m from the impact point reconstructed bhy the telescope.

Then we used the Chewie software to link the triggered events collected from the minimodule to the tracks reconstructed by Monicelli, so to evaluate the efficiency and the resolution of the 2S module. A triggered event was only accepted if there was only 1 track passing through the minimodule during that trigger.

## 3.2 Calibrations

The first analysis I performed regarded the calibration of the detector.

When a silicon detector is supplied with a bias voltage, a small leakage current is always measurable. Furthermore the mean value of this current is different for each channel, so it needs to be equalized, so that the results output from different channels are coherent. I determined the distributions of these current pedestals, after the equalization and, by doing so, I could also determine the distribution of the noise of the detector. This is done by fitting with an error function the S-curve of every channel: the mean of the fit is taken as pedestal value, while the sigma represents the noise of the channel. An example of S-curve is shown in 3.2:

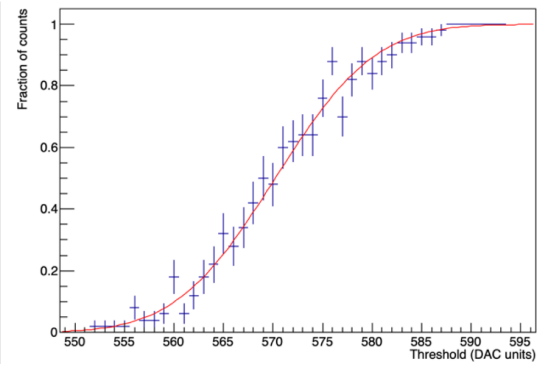


**Figure 3.2:** An example of S-Curve fitted with an error function (in red)

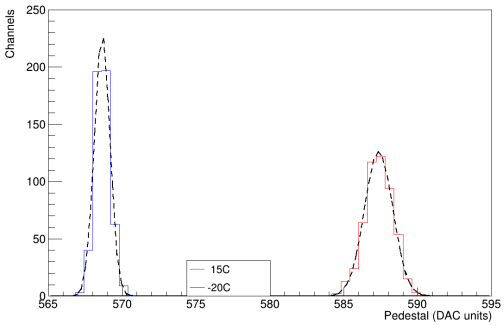


**Figure 3.3:** Positions of the pedestal for the unirradiated sensor at different temperatures.

it is obtained by measuring the ratio between hits detected without beam and the number of software triggers provided to the chip, at various signal thresholds.

The result, for the unirradiated sensor, is shown in figure 3.3, where we also can see that the pedestal changes its position at different temperatures.

Furthermore, figure 3.4 shows how the noise mean value decreases with decreasing temperature, thanks to the decrease of the thermal noise.

In figure 3.5 it is shown the important result that the noise mean value does not change with the irradiation until the last data taking period. However, even at full irradiation, it increases of only 1 DAC unit, though the corresponding noise distribution displays a more pronounced dispersion.

## 3.3 The Preliminary Scans

After the calibrations, I analyzed the data regarding some preliminary timing scans, in order to review the choices during the test beam and to improve what will be done in future test beam runs.

At first, I analyzed how the efficiency of the sensor changed with the latency of the chip (fig. 3.6), to determine the correct delay, in clock units, between the arrival of the particle onto the detector and the receiving of the trigger by the readout chip. For the unirradiated sensor, the optimal latency was 35 clock units.

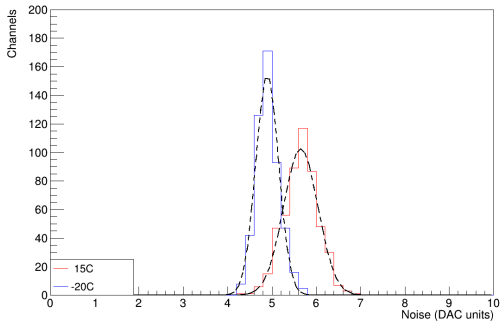


**Figure 3.4:** Distribution of the noise for the unirradiated sensor at different temperatures. It is noticeable how the noise mean value decreases when temperature decreases.

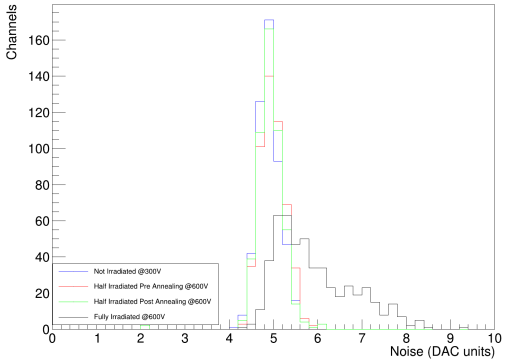


**Figure 3.5:** Summary of the noise distributions for the different data taking periods. The noise mean value never changed until the last data taking period.

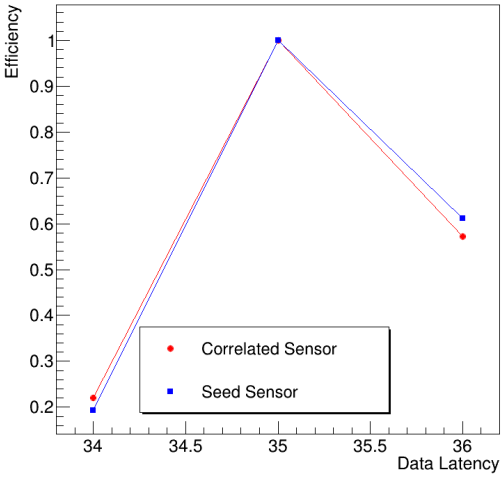


**Figure 3.6:** Example of latency scan. It refers to the unirradiated sensor.

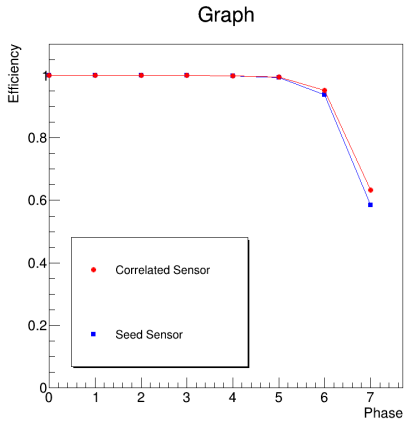


**Figure 3.7:** Example of phase scan. It refers to the unirradiated sensor.

To have a better latching of the chip clock with the arrival of the particle, for the first two data taking periods it was used a function of the chip which allowed the clock to be divided in eight different phases, each one lasting 3.125 ns, so I also analyzed the phase scans. For the unirradiated sensor (fig. 3.7), the optimal phase was 0.

For the test beam of December 2018, a delay-locked loop (DLL) was used to scan the phase of the chip clock. A DLL is a device which can latch to an external clock, recreate it with a different phase and supply it to other devices. The resolution of the DLL is 1 ns, so it was possible to divide the chip clock in 25 phases. The phase scan obtained with the DLL is shown in figure 3.8, where the 0 of the phase refers to a latency of 41 clock units, which was the one resulting from the latency scan. It is possible to see that there is a plateau of maximum efficiency. Nevertheless, this information is not enough to choose the right phase.

In order to solve this issue, I decided to analyze also how the cluster mean size varies with the clock phase. The cluster size is the number of strips that are fired in a cluster. A cluster size greater than 1 is due to charge sharing between adjacent strips. Because of this, greater cluster sizes are smaller and stay over threshold for less time than signals coming from a cluster of size 1. According to this, the optimal value of the phase should be the one which maximizes the cluster mean size, as this case means that we are also collecting the hits from smaller signals. The optimal phase can then be chosen from the plot in figure 3.9 which shows clearly a maximum around 4 ns.

## 3.4 The Stub Efficiency

An important goal of this data analysis was to check the proper functioning of the stub logic, so to verify the efficiency of the $p_T$ threshold. As mentioned in chapter 2, the $p_T$ of the particle determines the the value of the azimuthal component that its path acquires in a magnetic field. So, we could simulate a variation of the $p_T$ of the particles by tilting the minimodule, so to artificially provide trajectory of the particle with a component along $\phi$ (fig 3.10).

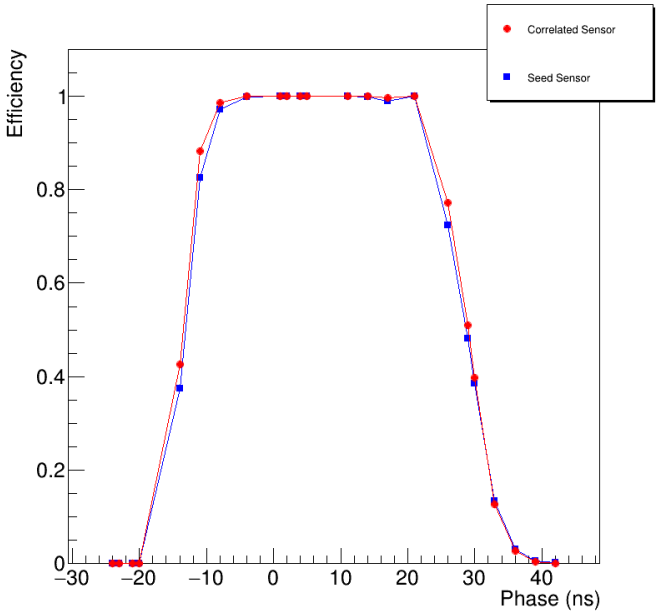


**Figure 3.8:** Phase scan obtained using the DLL. It refers to the fully irradiated sensor.

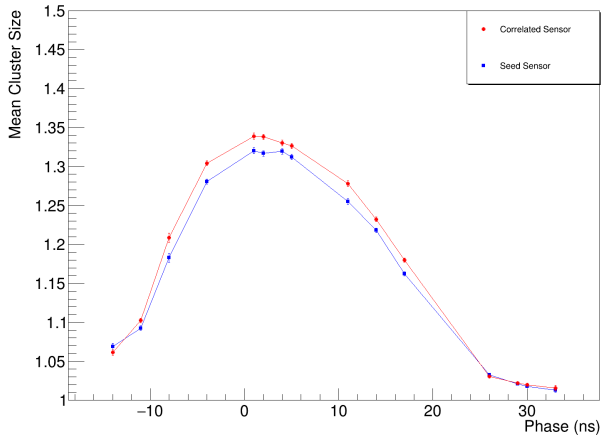


**Figure 3.9:** Phase scan of the mean cluster size. It refers to the fully irradiated sensor and show that the optimal phase for the this test beam would have been around 4 ns.

The formula used for the conversion between the simulated $p_T$ and the tilting angle $\beta$ is:

$$\sin\beta = \frac{r}{2R} \tag{3.1}$$

$$R = \frac{p_T}{qB} \tag{3.2}$$

where, once again, $R$ is the radius of curvature of the particle and $r$ is the distance of the module from the beampipe.

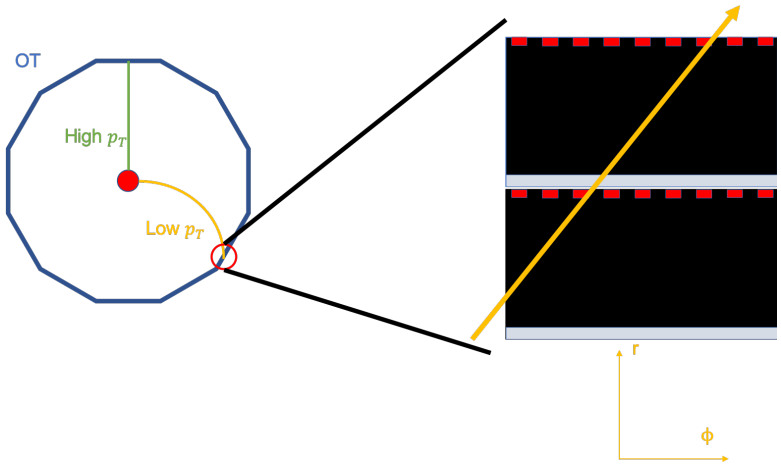


**Figure 3.10:** A particle emitted with a low $p_T$ passes through the detector with a considerable angle with respect to the radial direction.

The results, shown for the unirradiated sensor, are presented in figure 3.11 and shows a fairly net cut in efficiency around a chosen tilting angle. It also evident that the threshold can be chosen by adjusting the maximum distance between the clusters on the two sensors in the minimodule.

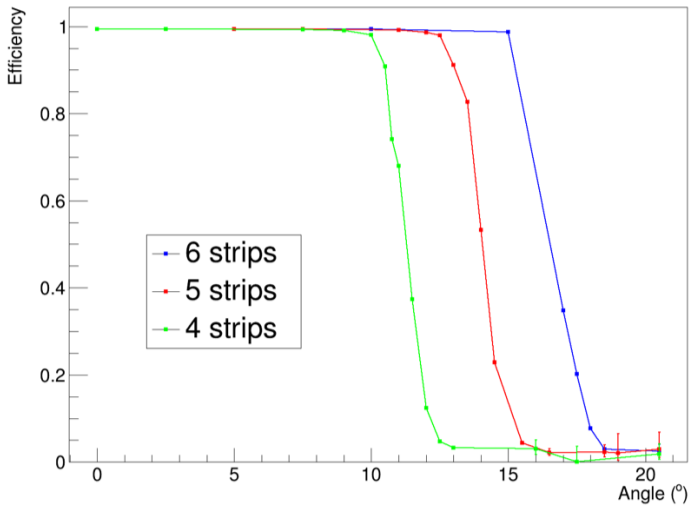


**Figure 3.11:** Efficiency of the sensor with respect to the tilting angle of the minimodule for different maximum distance between the clusters.

Using the formula 3.2, we also converted the plot in figure 3.11 to the a scan of the efficiency in function of the simulated $p_T$ of the particle tracked (fig. 3.12). We observed that the threshold applied to the $p_T$ was compatible to the one calculated with the relation 2.2

This study showed us the effectiveness of using the stub logic for the L1 Trigger.

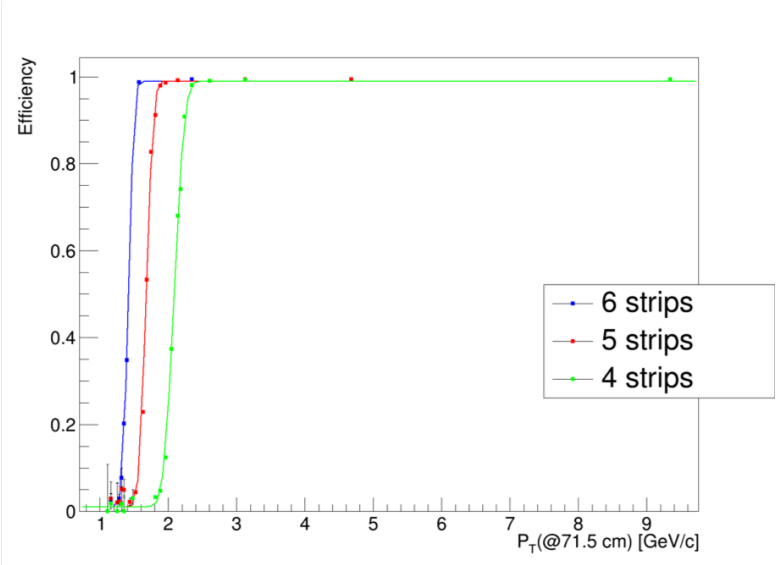


**Figure 3.12:** Efficiency of the sensor as a function of the $p_T$ of the tracked particle for different maximum distance between the clusters.

## 3.5 The Threshold Efficiency

One of the most important things to verify with these test beam runs was to verify that the sensor had a good efficiency even after being irradiated with a conspicuous fluence of radiation. To do this, I produced the summary shown in figure 3.13, which shows that even when fully irradiated, the sensor still has high efficiency at the thresholds which should be used in CMS.

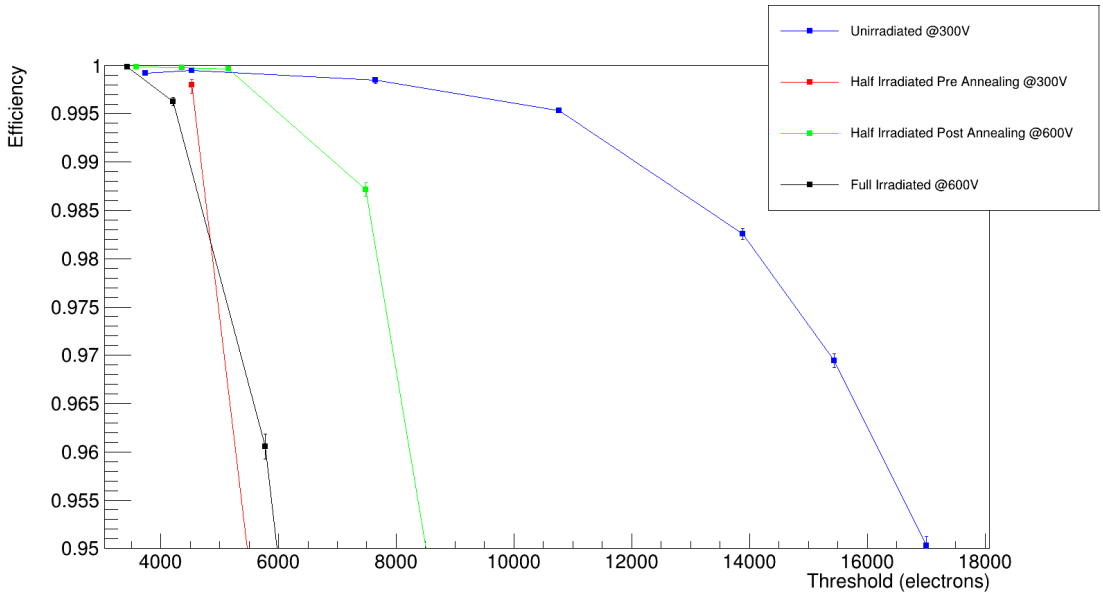


**Figure 3.13:** Summary of the efficiency of the sensor for each data taking period.

We wanted to obtain more information on the performance of the detector, so we analyzed thoroughly how the efficiency changes with the threshold. Given the binary logic of the readout chip, what we obtained is the curve which shows the fraction of events when more than a certain charge was collected in the detector, i.e., the cumulative distribution function of the charge collected. We, then, fitted the experimental data and obtained a Landau-Gauss convolution, which represents the probability distribution function of the charge collected (fig. 3.14).

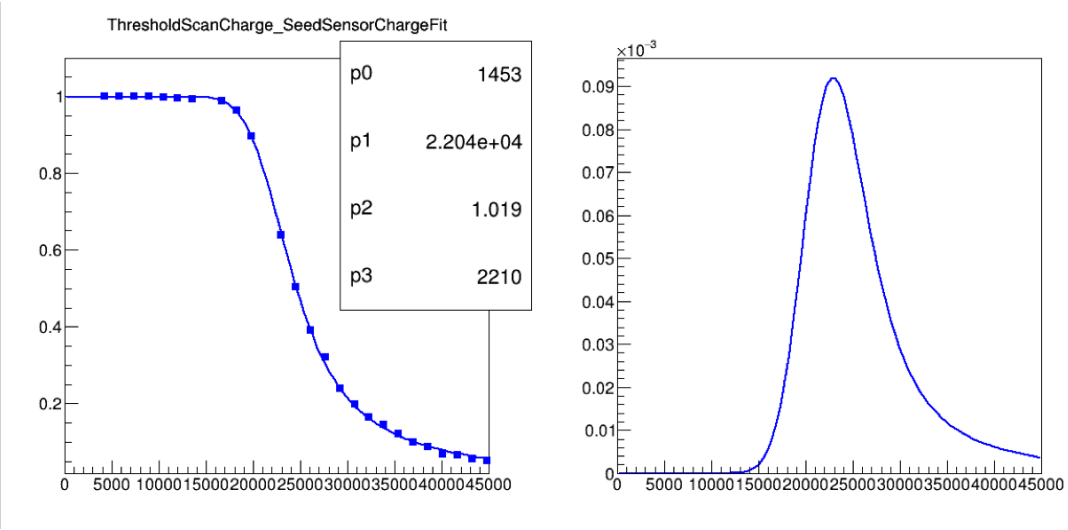


**Figure 3.14:** The left plot shows how the efficiency changes with the threshold and the right picture shows its derivative, which represents the probability to collect a certain amount of charge in an event. This plots refer to the unirradiated seed sensor.

The Gauss curve in the convolution should account for the electric noise of the detector itself, whose value we measured to be far from the 2210 electrons of the fit (p3 in figure 3.14). In fact, from the calibrations, for the unirradiated sensor we obtained a value of 882 electrons. By fixing p3 to this value, we obtain the fit in figure 3.15, which is still in agreement with the experimental data, except for the tail, where the fit is higher.

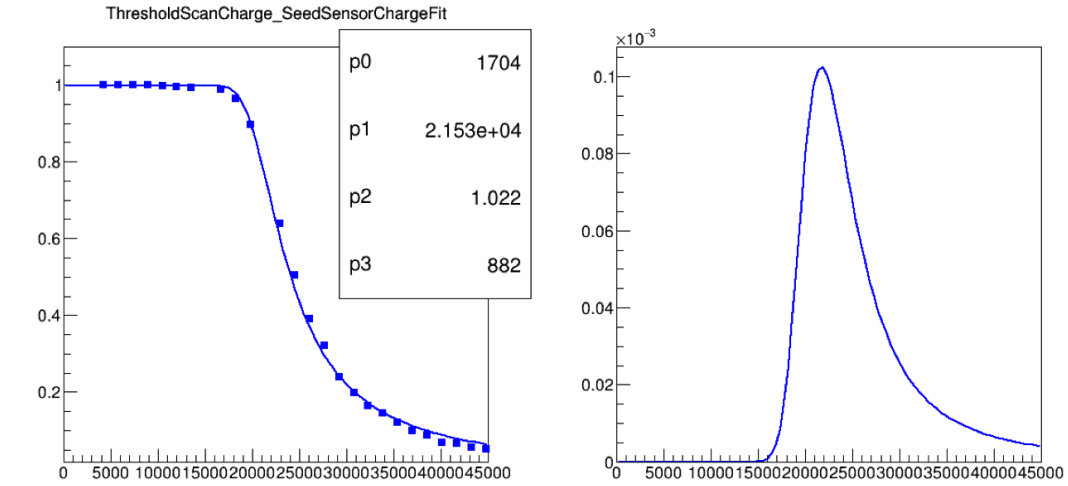


**Figure 3.15:** Fit of the Landau-Gauss curve obtained by fixing the standard deviation of the gaussian at 882 electrons.

We thought this could be due to $\delta$-rays, highly-ionizing electrons emitted in the bulk of the sensor which release their charge far from the primary track and create large clusters (fig. 3.16).

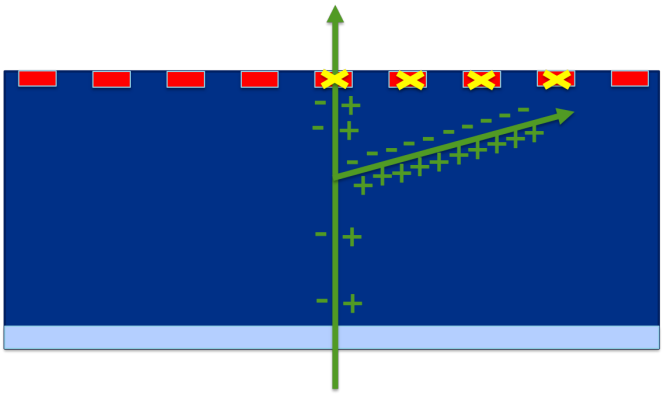

**Figure 3.16:** $\delta$-rays tend to release charge spreading it on multiple strips.

Our idea is that only $\delta$-rays are ionizing enough to release high amount of charges, but some of them we may be neglecting because of their tendency to spread the charge released between multiple strips.

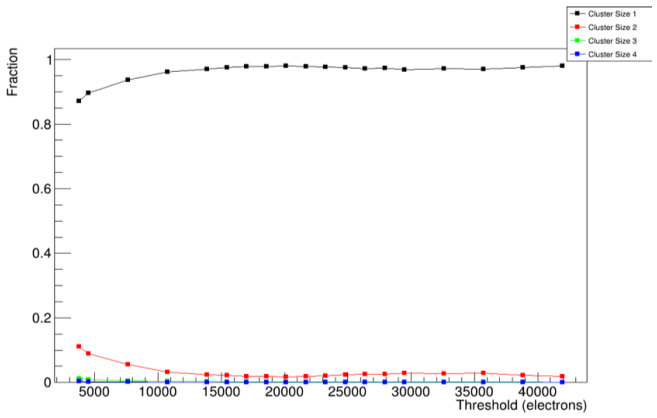


**Figure 3.17:** The plot shows how the fraction of clusters of a certain size changes with the threshold applied to the detector.

To verify this, I produced the plot in figure 3.17, which shows the fraction of clusters of a certain size as a function of the threshold. At high thresholds, we expected the fraction of size 2 clusters to decrease rapidly, as it implies that the two strips both collect a signal above threshold. Instead, we observed a small rise in the fraction of size 2 clusters, which could be due to the fact that at high thresholds what we see are mostly $\delta$-rays.

Because of this, the Landau-Gauss fit closer to the physical reality should be the one with the fixed standard deviation of the gaussian. Nevertheless, the Landau's MPVs (most probable values)in the two cases differ for only $\sim$500 electrons.

We used the Landau-Gauss fits (without fixing the sigma) to describe the performances of the sensor in the various test beam runs, and obtained the plot in figure 3.18.

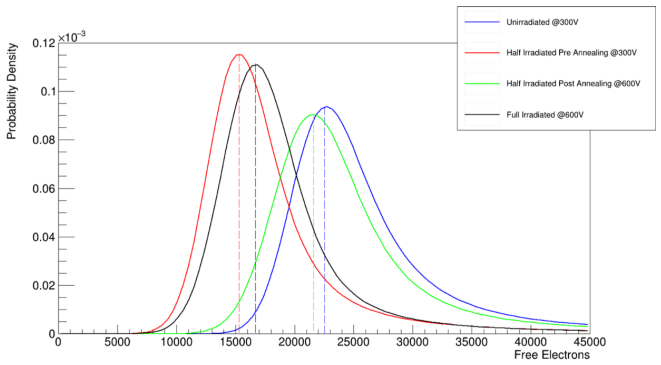


**Figure 3.18:** Summary of the Landau-Gauss fits of the sensor for each data taking period.

As we expected, the irradiation damage causes a decrease in the number of electrons collected and this is reflected in a negative shift of the Langauss curve. It is also noticeable that we can use the MPV of the curve as a parameter to characterize the performance of the detector, thus obtaining the summary in figure 3.19.

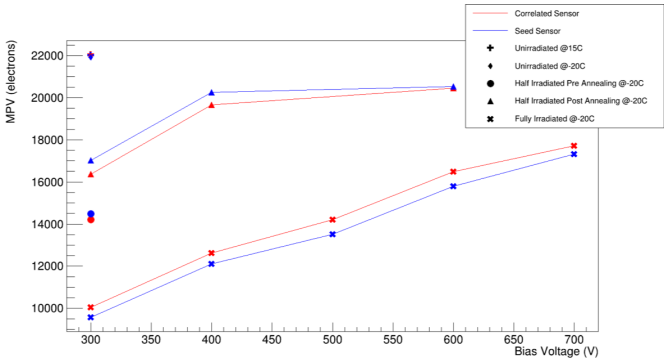


**Figure 3.19:** Summary of the MPVs of the charge collected by the sensor for each data taking period.

We can conclude that even at high integrated luminosity, the sensor has high efficiency, as long as the bias voltage is increased with the aging of the sensor, and we also noticed that our results are compatible with the literature.[7]

# Conclusion

In this report I talked about my 2-month long experience at Fermilab. The main work I had to carry out was the data analysis of the three test beam runs described in this report itself, in order to describe the radiation hardness of the 2S module and the effectiveness of using the tracker information at L1 Trigger. I worked in a stimulating environment to a challenging task, which I completed independently and in exhaustive fashion, with constant feedback from my supervisor.

After two months of work, I could compare the performance of the Outer Tracker module after different radiation doses and establish that the 2S Minimodule will still be efficient at the end of the lifetime of CMS.

The other important result I obtained is that the stub logic works as well as expected and will have a very important role after the CMS upgrade.

In conclusion, I think that this experience had great importance in my growth as a young scientist and the things I learnt will be valuable in my future career.

# Bibliography


[1] https://home.cern/science/accelerators/large-hadron-collider

[2] CMS Collaboration, *The Phase-2 Upgrade of the CMS Tracker Technical Design Report*

[3] G. Apollinari et al., *High-Luminosity Large Hadron Collider (HL-LHC): Preliminary Design Report*

[4] https://home.cern/science/experiments/cms

[5] https://cms.cern/detector

[6] CMS Collaboration, *CMS Technical Design Report for the Pixel Detector Upgrade*

[7] The RD50 Collaboration, *Radiation tolerant silicon detectors*

[8] Helmuth Spieler, *Lecture Notes* https://www-physics.lbl.gov/ spieler/physics_198_notes_1999/index.html